IEEE Access
Multidisciplinary ⋮ Rapid Review ⋮ Open Access Journal

Received August 21, 2020, accepted September 7, 2020, date of publication September 21, 2020, date of current version October 13, 2020.

Digital Object Identifier 10.1109/ACCESS.2020.3025715

Sparse Reconstruction-Based Inverse Scattering Imaging in a Shallow Water Environment

JINGNING JIANG, XIANG PAN, AND T. C. YANG

College of Information Science and Electronic Engineering, Zhejiang University, Hangzhou 310027, China

Corresponding author: Xiang Pan (panxiang@zju.edu.cn)

This work was supported in part by the National Natural Science Foundation of China under Grant 41776108, Grant 61531017, and Grant 61571397; and in part by the National Key Research and Development Program of China under Grant 2017YFC0306901.

ABSTRACT Bistatic sonar or multistatic sonar system can collect more scattering information of targets than a monostatic sonar system. In this paper, sparse learning via iterative minimization method (SLIM) is introduced to distinguish wave components for time-domain (TD) back-propagation (BP) inverse scattering imaging improvement. Unlike the prevailing high central frequency (>100 kHz) and wideband imaging sonar systems, a relatively low-frequency band (1-10 kHz) is considered here. Due to the low sidelobe output of SLIM, the investigated object's surface in TD-BP image is much clearer in an ideal two-dimensional free field case. Furthermore, when the environmental information is known, this sparse reconstruction-based channel deconvolution method can be implemented to recognize, categorize the main propagating paths and then rectify their time of arrivals. Compared with the phase conjugation-based channel deconvolution method, the proposed approach's results have fewer sidelobes and higher signal-to-background ratio in the simulation.

INDEX TERMS Acoustic imaging, sparse reconstruction, inverse scattering, waveguide environment.

I. INTRODUCTION

Active acoustic imaging is the technique to locate an object's scattering strength distribution and characterize it. An acoustic color image or a tomography imaging result can be generated by actively scanning an object from various view directions or aspect angles.

An acoustic color image displays the angle-frequency spectrum of an object manifesting its scattering characteristics. Firstly, an acoustic color image is used to verify and validate the theoretic model with the experimental measurements. For example, a cylindrical shell's acoustic color has been studied, where the striations and structures in the image are associated with the elastic waves [1] or the internal structures [2]. Moreover, when the object is placed near a horizontal surface, the acoustic color images are considered, and the ray-based model [3]–[5], finite element model [6], and three-dimensional/hybrid models [7], [8] were developed to match their corresponding experimental configurations. The acoustic color image of the observed elastic waves can be generated by using fractional Fourier transform to separate each wave component [9]. After that, acoustic color images are also used for object classification and target identification [10], [11] because objects of different shapes or materials exhibit different scattering responses. Aside from object identification, the acoustic color images will help to determine the aspect angle of a cylinder [12].

The acoustic tomographic imaging technique often densely collects scattering information and maps the time series data to spatial scattering strength distribution. We treat the synthetic aperture sonar (SAS) imaging as one type of acoustic tomographic imaging for similar data acquisition and processing methods. An acoustic tomographic imaging system often adopts a high center frequency (>10 kHz) and a broadband/wideband transmitted pulse. The back-propagation (BP) [13] method and Fourier reconstruction method are used in a reflection tomographic imaging case [14], to reveal the geometric shape and highlight points. Acoustic tomographic imaging, or SAS imaging, can make the multiple scattering phenomena more apparent in the spatial domain [7], [15], [16]. Acoustic quasi-holographic images better reveal each wave component's features, such as propagation time and occurring position, as well as multiple scattering between objects [17], by back-propagating the time series data to a fixed plane then display the image along time and cross-range axes. Other than the mentioned methods,

The associate editor coordinating the review of this manuscript and approving it for publication was Yunjie Yang.

the linear sampling method (LSM) [18] is also applied in the underwater object imaging task with the partial frequency variation approach [19]. LSM, unlike acoustic tomographic methods, calculates the indicator function to mark whether a pixel/voxel is within the scatterer.

The literature listed above does not involve a multipath/multi-mode propagation effect in an underwater waveguide. It needs to deconvolve the channel impulse response (CIR) first. The acoustic color assisted by the holographic technique shows the differences among a rigid sphere, a soft sphere, and a directional source [10]. Target imaging is also numerically performed in a range-depth waveguide [20], [21] through DORT (decomposition of the time-reversal operator) and BP.

Compressive sensing or sparse reconstruction method is widely used in underwater acoustics [22], especially in the field such as direction of arrival (DOA) estimation [23]–[25], CIR estimation [26], [27], and near-field acoustic holography [28], [29]. However, seldom underwater acoustic imaging works are under the compressive sensing framework. The alternating direction method of multipliers (ADMM) has been used for distributed optimization to improve the resolution of SAS images. Similarly, ADMM is applied to solve multi-frequency far-field equations simultaneously in LSM imaging [19].

The main contributions of this paper include: (1) Through the classical back-propagation inverse scattering processing (ISCP) method, a time-domain (TD) back-propagation (BP) scheme is used here to avoid arduous work at each frequency. Furthermore, the TD-BP combined with the SLIM method outputs a better image in two-dimensional free-field space. Also, the imaging process and its corresponding physics are connected. (2) Analyzes the impact of waveguide environmental parameters on defocusing and ghosting by the conventional ISCP method. A sparse reconstruction-based channel response deconvolution method is proposed to solve these adverse effects in the underwater waveguide.

This paper is organized as follows: Section II reviews the inverse scattering problem in a two-dimensional ideally free field case. The time-domain back-propagation method using the output of a matched filter (MF) or SLIM is presented and discussed. Section III studies the inverse scattering problem in a range-independent shallow water waveguide, where the multipath effect brings defocusing and ghosting into the image generated by the conventional BP algorithm. This sparse reconstruction-based channel deconvolution imaging is proposed to solve that problem. Section IV gives the conclusion.

II. ISCP IMAGING IN A TWO-DIMENSIONAL (2D) FREE FIELD SCENARIO

A. A GENERAL INVERSE SCATTERING IMAGING METHOD

The inverse scattering procedure using an acoustic or electromagnetic bistatic system can be modeled as Fig.1. In Fig.1, the center of a scattering object is set as the origin O. Then,

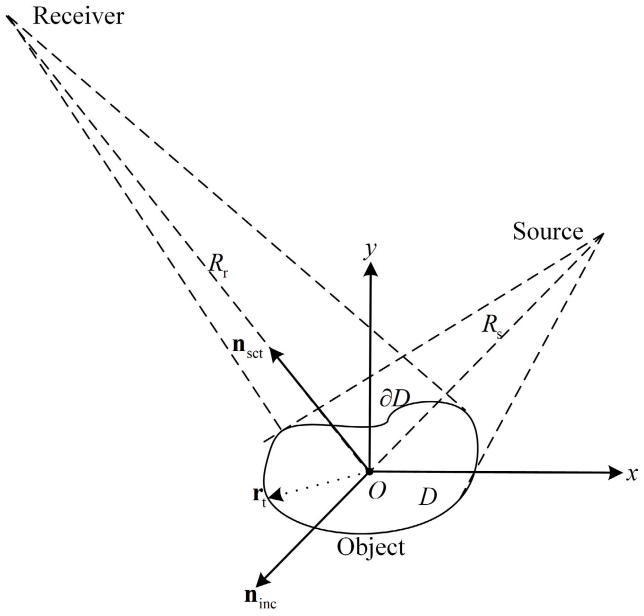

FIGURE 1. Schematic view of the inverse scattering imaging process.

the source's location is at $\mathbf{r}_{inc}$ with its distance to the origin O being $R_s = ||\mathbf{r}_{inc}||$. D is the scattering object with ∂D being its surface. The incident direction is $\mathbf{n}_{inc} = -(\cos\phi_{inc}, \sin\phi_{inc})$. Similarly, when the receiver moves at $\mathbf{r}_{sct}$, its distance to the origin point is $R_r = ||\mathbf{r}_{sct}||$ and the scattering direction is $\mathbf{n}_{sct} = -(\cos\phi_{sct}, \sin\phi_{sct})$. $\mathbf{r}_t$ is a point in the imaging area.

A classical inverse scattering method is the back-propagation (BP) method. The BP method needs first to convert the scattered pressure data $P(\mathbf{r}_{sct}; \mathbf{r}_{inc}, \omega)$ into a far-field pattern $f(\mathbf{n}_{sct}, \mathbf{n}_{inc}, \omega)$.

The far-field pattern f is dependent on the scattering direction $\mathbf{n}_{sct}$ and the incident direction $\mathbf{n}_{inc}$. The generalized Bojarski transform builds the relation between the far-field pattern and the shape of a scattering object through physical optical (PO) approximation [13].

$$\begin{aligned} B_g(\mathbf{n}_{sct}, \mathbf{n}_{inc}) &= f(\mathbf{n}_{sct}, \mathbf{n}_{inc}) + f^*(-\mathbf{n}_{sct}, -\mathbf{n}_{inc}) \\ &= \pm\frac{ik}{2\pi}\int_{\partial D_1} \mathbf{n}_{inc}\cdot\mathbf{n}_t e^{-ik(\mathbf{n}_{sct}-\mathbf{n}_{inc})\cdot\mathbf{r}_t} dS \\ &\pm \frac{ik}{2\pi}\int_{\partial D_2} \mathbf{n}_{inc}\cdot\mathbf{n}_t e^{-ik(\mathbf{n}_{sct}-\mathbf{n}_{inc})\cdot\mathbf{r}_t} dS \\ &= \mp\frac{1}{4\pi} \parallel k(\mathbf{n}_{sct}-\mathbf{n}_{inc}) \parallel^2 \\ &\quad \int \Gamma(\mathbf{r}_t) e^{-ik(\mathbf{n}_{sct}-\mathbf{n}_{inc})\cdot\mathbf{r}_t} dV, \end{aligned} \tag{1}$$

where indicator function $\Gamma(\mathbf{r}_t)$ only takes 1 when $\mathbf{r}_t$ is within the scatterer. The final $\mp$ in (1) is "+" for the case that the object has the rigid/Neumann boundary condition. It clearly shows B_g is the spatial Fourier transform of $-\nabla^2\Gamma(\mathbf{r}_t)$.

Therefore, the BP imaging [13]

$$\begin{aligned} I_{BP}(\mathbf{r}_t) = \pm\frac{k^2}{8\pi^2}\int_{\Omega_{inc}}\int_{\Omega_{sct}} B_g(\mathbf{n}_{sct}, \mathbf{n}_{inc}) \\ \times e^{ik(\mathbf{n}_{sct}-\mathbf{n}_{inc})\cdot\mathbf{r}_t} d\Omega_{sct} d\Omega_{inc} \end{aligned} \tag{2}$$

is to find the outer and inner bounds of a scatterer's boundary. In (2), Ω_{inc} is the aperture composed by different source positions, and Ω_{sct} is the aperture of receivers.

Usually, (2) can be relaxed to

$$I_{\text{BP}}(\mathbf{r}_{\text{t}}, \omega) = \int_{\Omega_{\text{sct}}} f(\mathbf{n}, \mathbf{n}_{\text{inc}}, \omega) \mathrm{e}^{ik\mathbf{r}_{\text{t}}\cdot(\mathbf{n}_{\text{inc}}-\mathbf{n}_{\text{sct}})} \mathrm{d}\Omega_{\text{inc}}, \quad (3)$$

where $\mathbf{r}_{\text{t}}$ is a pixel in the imaging area. The disadvantage of the BP method is that it has to process data of one frequency at each time.

In practical applications, the probing signal is a wideband waveform, and the imaging result can be directly gotten from the received time-domain signal $p(t)$ without the far-field pattern conversion:

$$I_{\text{TD-BP}}(\mathbf{r}_{\text{t}}) = \int_{\Omega_{\text{sct}}} \int_{\Omega_{\text{inc}}} p(t) \times \delta(ct - R_{\text{s}} - R_{\text{r}} - \mathbf{r}_{\text{t}} \cdot(\mathbf{n}_{\text{inc}} - \mathbf{n}_{\text{sct}})) \, \mathrm{d}\mathbf{n}_{\text{sct}} \mathrm{d}\mathbf{n}_{\text{inc}}, \quad (4)$$

where $\delta(\cdot)$ is the one dimensional Dirichlet function, c is the propagation speed in the medium. By reviewing Fig.1, it can be found that (4) uses the linearized approximation of $||\mathbf{r}_{\text{t}} - \mathbf{r}_{\text{s}}|| \approx R_{\text{s}} + \mathbf{n}_{\text{inc}} \cdot \mathbf{r}_{\text{t}}$, and $||\mathbf{r} - \mathbf{r}_{\text{t}}|| \approx R_{\text{r}} - \mathbf{n}_{\text{sct}} \cdot \mathbf{r}_{\text{t}}$. This indicates (4) is originated from the time domain delay-and-sum expression:

$$I(\mathbf{r}_{\text{t}}) = \int_{\Omega_{\text{sct}}} \int_{\Omega_{\text{inc}}} p(t) \cdot \delta(t - ||\mathbf{r}_{\text{t}} - \mathbf{r}_{\text{s}}||/c - ||\mathbf{r} - \mathbf{r}_{\text{t}}||/c) \, \mathrm{d}\mathbf{n} \mathrm{d}\mathbf{n}_{\text{s}}. \quad (5)$$

Ideally, (5) should also produce peaks indicating the outer bound and the inner bound of an object's surface as (2). Hereafter, this paper uses BP's time-domain equivalence (5) to output the inverse scattering imaging results.

B. SOUND SCATTERING AND INVERSE SCATTERING IMAGING IN A 2D FREE FIELD

Here, we study the inverse scattering imaging of an infinite long rigid cylinder in a 2D free field. The scattering response $S(\omega)$ of an infinite long rigid cylinder with radius a is well studied, that

$$S(\phi_{\text{inc}}, \phi_{\text{sct}}, \omega) = \sum_{n=-\infty}^{\infty} \frac{J_n'(ka)}{H_n^{(1)\prime}(ka)} H^{(1)}(kr) \mathrm{e}^{in(\phi_{\text{sct}}-\phi_{\text{inc}})} \quad (6)$$

where J_n and $H_n^{(1)}$ are the nth order of Bessel function and Hankel function of the first kind respectively. In the time domain, $S(\omega)$ corresponds to a specular reflection wave and creeping waves through the Sommerfeld-Watson transformation [30]. Their propagation paths are depicted as Fig.2 and their propagation time t_{sr} (specular reflection) and t_n (for the nth creeping wave) are:

$$t_{\text{sr}} = \frac{R_{\text{s}} + R_{\text{r}} - 2a\sin(|\phi_{\text{sct}} - \phi_{\text{inc}}|/2)}{c} \quad (7)$$

$$t_n(ka) = \frac{R_{\text{s}} + R_{\text{r}}}{c} + \frac{a\,||\phi_{\text{sct}} - \phi_{\text{inc}}| + 2n\pi|}{c_l(ka)} \quad (8)$$

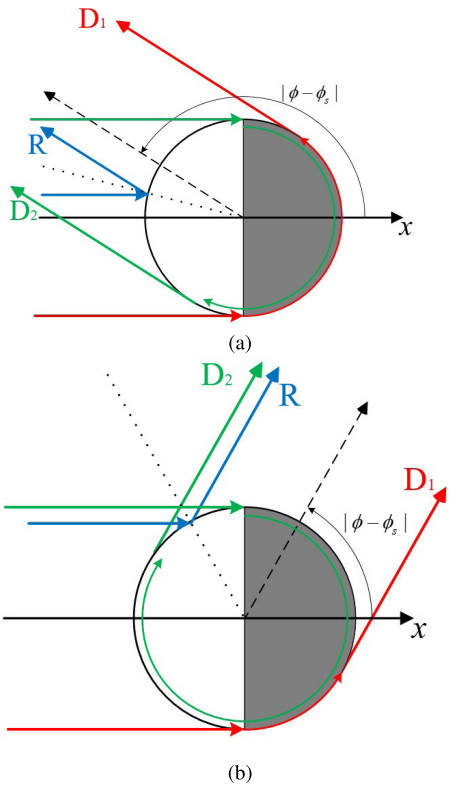

FIGURE 2. The schematic diagrams of an infinite long rigid cylinder's scattering process when illuminated by a normal incident wave (toward $+x$ direction) [30]. (a) Backward scattering case; (b) Forward scattering case. The blue line "R" is the path of reflection wave. The red line "D_1" is the counterclockwise propagated creeping waves ($n \geq 0$ in (8)). The green line "D_2" is the clockwise propagated creeping waves ($n < 0$ in (8)).

where

$$c_l(ka) \approx c\left[1 + 0.5 \cdot 6^{1/3}(ka)^{2/3} q_l\right]^{-1} \quad (9)$$

is the creeping wave's propagation speed on the cylinder's surface. In (8), $n \in \mathbb{Z}$, and $n \geq 0$ represents the anticlockwise propagation direction while $n < 0$ is the clockwise direction. The strength of these two waves can be found in [30], and not discussed here.

C. SIMULATION IN 2D FREE FIELD SPACE

To illustrate how the inverse scattering imaging works, a simulation is built as Fig.3. In Fig.3, a 0.5 m-radius rigid cylinder is located at ($x = -1$ m, $y = 1$ m), and the source stays at ($x = 20$ m, $y = 20\sqrt{3}$ m). The source emits a 10 ms long, 3-9 kHz up-sweep Tukey windowed linear frequency modulation (LFM) pulse, while a receiver moves circularly on a 40 m-radius circle ($R = 40$ m). The sound speed is 1500 m/s. The pressure field is generated by the μ-diff toolbox [31].

The creeping waves are more likely to be observed at the forward scattering zone that $|\phi_{\text{sct}} - \phi_{\text{inc}}| < 90°$. Thus, Fig.4 depicts the envelopes of matched filtered received data when the receiver is at the interval of 150° to 330°. The simulation data perfectly matches the time of arrivals (TOAs) of specular

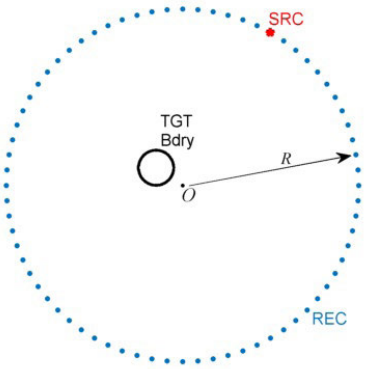

FIGURE 3. The simulation configuration. The red star marks the source's position ($x = R\cos 60°, y = R\sin\ 60°$), where $R = 40$ m. A 0.5 m radius rigid cylinder (black circle) is set at ($x = -1$ m, $y = 1$ m). The blue dots denotes the trajectory of a moving receiver.

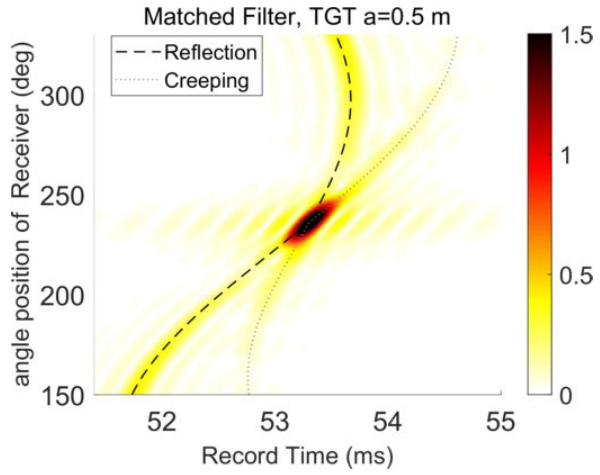

FIGURE 4. Matched filter results when the receiver is at angles from 150° to 330°. The black dashed line denotes the predicted reflection waves' time of arrival (TOA), while the green dotted line is the predicted creeping waves' TOA. In this receiving angle interval, creeping waves suffer less attenuation.

reflection (black line) and the creeping wave (green line). Besides, when $|\phi_{\text{sct}} - \phi_{\text{inc}}| < 5°$, the scattering amplitude is far higher than other receiving angles, which displays as the brightest spot in Fig.4.

The next part is to transform the received time-series data into the ISCP image. Fig.5 is the superposition of transformed images from several selected receiving angles from Fig.4. Each bright ambiguity line in Fig.5 is tangent to the cylinder's surface (the white dashed circle), which is the same as the conventional mono/bi-static sonar's image. In Fig.5, all noticeable parts are marked by white numbers. "1" represents the lines formed by reflection waves when the receiver is at the 150°-200° interval, while "2" corresponds to the case when the receiver is within 270°-330°. These nearly straight lines have neighboring points of tangency and forming a superposition region numbered as "4". "5" is the counterpart for "2". "3" an "X"-shaped pattern, is the intersection of reflection waves' (1 and 2 in Fig.5) from selected observation angles.

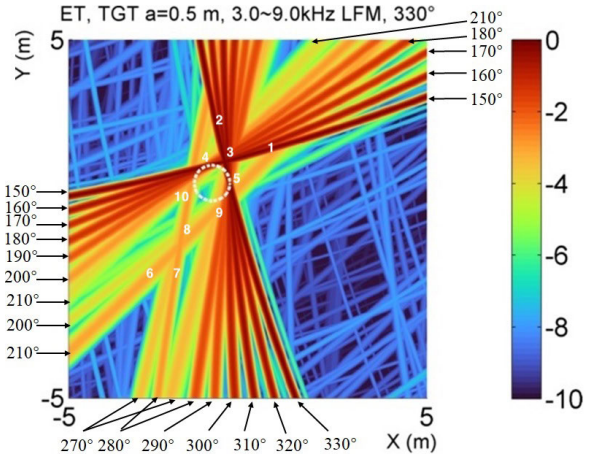

FIGURE 5. The superposition of inverse scattering results from selected receiving angles. The white dashed line circle is the boundary of the rigid cylinder. The ambiguity lines are marked by their corresponding receiving angles. The contribution of creeping waves is noticeable when the receiver is at 200°, 210°, 270° and 280°.

The creeping waves have a similar result. "6" is the belt formed by creeping waves accompanied by "1". The reason why "6" does not appear significant ramifications as "1" in Fig.5 is that the TOAs of creeping waves in Fig.4 are linearly dependent on $|\phi_{\text{sct}} - \phi_{\text{inc}}|$ as in (8), while the reflection waves' TOAs involves the sine of $|\phi_{\text{sct}} - \phi_{\text{inc}}|$. The creeping waves also generate a weaker "X"-pattern ("8") and have two points of the tangent ("9" and "10").

Thus, it can easily review Fig.6, the coherent summation using (5). When having data from only the first observation angle, the image result Fig.6(a) is mainly two ambiguity lines (reflection wave forms line "1" while creeping wave generates "6") tangent to the cylinder's surface. Also, there exist other ambiguity lines parallel to and nearby "1" being the sidelobes of "1". Lines lagging behind "6", on the other hand, are associated with high order creeping waves which are largely weaker than "6". Fig.6(b) shows the ambiguity lines "1" and "6" shrink to long spots "4" and "9"on the cylinder surface. Sidelobes and high order waves can not leave a coherent enhancement in Fig.6(b). As the receiver provides more observed data, "4" and "9" in Fig.6(c), shrinks toward curves along the cylindrical surface and an obscure. Besides, as the bi-scattering angles decreasing, "9" becomes brighter alongside with stronger creeping wave component.

Fig.6(d) and Fig.5 have more similar structures, that: the "X"-shaped patterns "3" and "8"; the curve "4" (the intersection of reflection waves) and "9" (that of creeping waves); as well as an obscure spot "10". Because data from small bi-scattering angles ($\mathbf{r}_t \cdot (\mathbf{n}_{\text{inc}} - \mathbf{n}_{\text{sct}}) \to 0$) are also taken into account, Fig.6(d) also displays a wide and strong ambiguity belt that emerges across the cylinder. Fig.6(e) shows the image accumulating all data in Fig.4, which adds "5" the reflection waves' contribution within 245°-330° and strengthens "3", "8" and "10". In the zoom-in part of Fig.6(e), Fig.6(f), "4", "5", "9" and "10" build outer

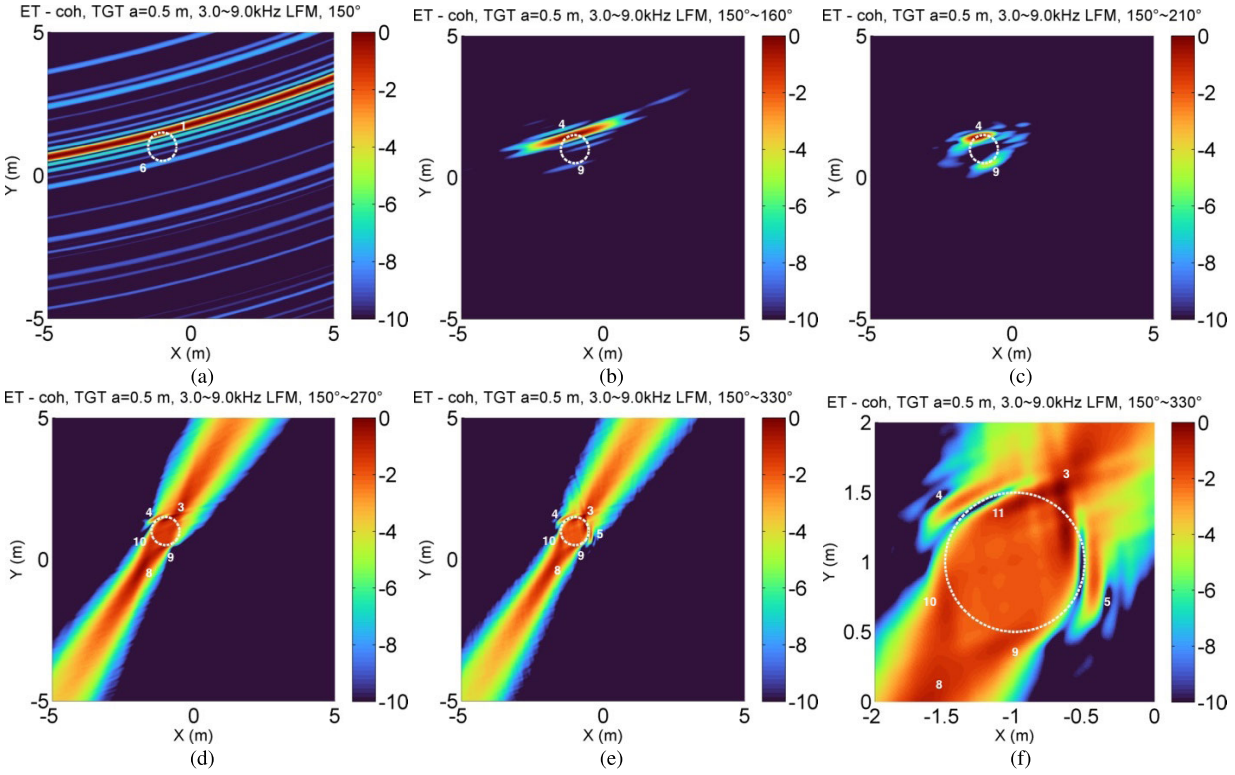

FIGURE 6. The coherent sum results as the receiver start from 150°. (a) Only use data received at 150°; (b) Adding up to 160°; (c) Adding up to 210°; (d) Adding up to 270°; (e) Adding up to 330°; (f) Zoom in of (e) around the cylinder.

edges of the cylinder's surface, while "3" contains more parts associated with inner edges. Fig.6(f) is in agreement with (2) which TD-BP method finds $|\nabla^2\Gamma(\mathbf{r}_t)|$.

Fig.6 exhibits the ISCP imaging using data collected from forward scattering direction (Fig.4), that $\mathbf{n}_{\text{sct}} \cdot \mathbf{n}_{\text{inc}} > 0$. The final recovered image only yields two clear segments of the outer boundary ("4" and "9" in Fig.6(f)), obscure segments of the outer boundary ("9" and "10") and the inner boundary ("11"). The limited receiving aperture lets Fig.6(f) deviate from (1) and (5). In Fig.7, receiving aperture ranges from 0° to 360°. Data collected when the observation angle is near to 246° will contribute to a strong ambiguity belt along "3" and "8", thus not used in imaging. By zooming-in, the detailed part of Fig.7(a), Fig.7(b) shows a clearer outer boundary "4" and inner boundary "11" generated by reflection waves as well as retains outer boundary "9" and "10" from creeping waves. However, sidelobes from reflection waves' MF output yield an inner spot "12" as well as ripples inside and outside the cylindrical surface. Fig.5-Fig.7 altogether, show the ISCP imaging in free-field space and prove that the BP method outputs $|\nabla^2\Gamma|$, an inner and outer boundary along the target surface as (1) and (5) predict.

D. SPARSE RECONSTRUCTION BASED IMAGING METHOD

By reviewing Fig.4 and Fig.7(b), it can be found that: (1) The output of MF has a wide main lobe, which may not well separate the reflection and creeping wave (because a windowed 3-9 kHz LFM pulse, the time resolution of MF is larger than 0.167 ms); (2) TD-BP using the output of MF produces lots of unwanted ripples and sidelobes. The sparse learning via iterative minimization (SLIM) [32] algorithm is used for a higher time resolution and imaging quality enhancement, as in Fig.8, when processing the same data as Fig.4. In Fig.8, the sidelobes near the receiving angle 246° are eliminated, and the wave structures are clearer.

It should be noticed that, when using SLIM, an implicit assumption is made that the frequency dispersion is neglectable. Here, for the 3-9 kHz bandwidth in use, according to (9), c_l ranges from 1181 m/s to 1327 m/s. On the other hand, in two-dimensional free-field space, the cylindrical spread wave propagation causes a $\sqrt{kR}$ attenuation, which will reduce the impact of creeping waves' dispersion. Also, the propagation distance that waves go through will not make a big difference.

Fig.9 exhibits the BP imaging output using SLIM processed data. The overall structure in Fig.9(a) is almost the same as Fig.7(a), while their zoom-in parts exist some differences. The inner and outer boundaries "4" and "11" are narrowed for the high time-delay resolution offered by SLIM. Besides, SLIM eliminates the number of sidelobes in MF output as well as lower their sidelobe levels, making the inner spot "12" and ripples in Fig.7(b) disappear. One can see that the sidelobe level is at least 2dB lower in Fig.8. The ambiguity belt is also alleviated in Fig.9.

Nevertheless, SLIM boosts the time-delay resolution at the cost of neglecting low amplitude components. Compared with Fig.7(a), the length of the inner/outer boundary is shorted. This is caused by some low energy peaks dropped by SLIM.

III. ISCP IMAGING IN A THREE-DIMENSIONAL (3D) RANGE-INDEPENDENT WAVEGUIDE

A. SCATTERING AND INVERSE SCATTERING IMAGING

In a shallow water waveguide, we use the Ingenito model [33] to study the sound scattering by simple shape targets. Following the Ingenito model, when given a rigid sphere's scattering function S in free-field space and the coordinates of the source($\mathbf{r}_{\text{inc}} = (r_s, \phi_s, z_s)$), target($\mathbf{r}_t = (0, 0, z_t)$), and receiver($\mathbf{r}_{\text{sct}} = (r, \phi, z)$), the scattered pressure P_{sct} can be expressed as

$$\begin{aligned} &P_{\text{sct}}(\mathbf{r}, \mathbf{r}_s; \mathbf{r}_t, \omega) \\ &= \frac{i}{4\rho(z_s)\rho(z_t)k} \sum_{m=1}^{\infty}\sum_{m'=1}^{\infty} \psi_{m'}(z_s)\psi_m(z) \frac{e^{ik_{rm'}r_s + ik_{rm}r}}{\sqrt{k_{rm'}r_s k_{rm}r}} \\ &\quad \times \left\{ \left[\psi_m(z_t)\psi_{m'}(z_t) - \frac{\psi'_m(z_t)\psi'_{m'}(z_t)}{k_{zm}k_{zm'}} \right] \right. \\ &\quad S(\gamma_m, \phi; \gamma_{m'}, \phi_s) \\ &\quad \left. + \left[\psi_m(z_t)\psi_{m'}(z_t) + \frac{\psi'_m(z_t)\psi'_{m'}(z_t)}{k_{zm}k_{zm'}} \right] \right. \\ &\quad \left. S(\gamma_m, \phi; \pi - \gamma_{m'}, \phi_s) \right\} \end{aligned} \tag{10}$$

where scattering function S is

$$S_{\text{rigid}}(\theta, \phi; \theta_s, \phi_s) = i \sum_n \frac{j_n(ka)}{h_n(ka)} (-1)^n (2n+1) P_n(\cos\beta). \tag{11}$$

In (11), the solid angle β can be determined from $\cos\beta = \cos\theta\cos\theta_s + \sin\theta\sin\theta_s\cos(\phi_s - \phi)$.

The reason why a rigid sphere is used here instead of a depth-extended cylinder in Sec.II, is: (1) The creeping waves' propagation speed on the sphere is a little slower than the cylinder's c_l [34] for nth-order spherical Bessel function $j_n(x) = \sqrt{\pi/(2x)}J_{n+1/2}(x)$, meaning their speed difference is $c_l^2/(2kac + c_l)$; (2) In free field space, the cylinder's scattering function has a vertically standing wave term

$$\int_{-L/2}^{L/2} e^{ik_z z} \sin[k_p(z + L/2)]\mathrm{d}z \tag{12}$$

Correspondingly, in the waveguide, after plugged that into the Ingenito model, it gives

$$\begin{aligned} &N_{m'}^{-}\left[\int N_m^{-} e^{ik_{zm}z} \sin(k_p z) dz \right. \\ &\quad \left. - \int N_m^{+} e^{-ik_{zm}z} \sin(k_p z) dz \right] \sin(k_p z) \\ &= N_{m'}^{-} \sin(k_p z) \int \psi_m(z) \sin(k_p z) dz \end{aligned} \tag{13}$$

The integral in (13) plays a model selection role.

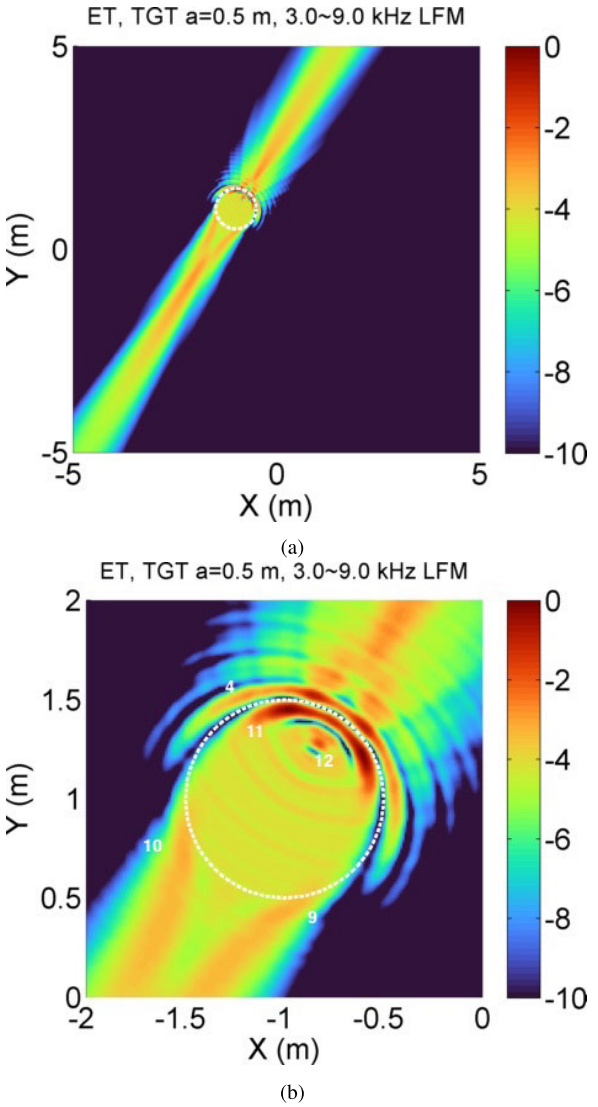

FIGURE 7. The complete inverse scattering result after the receiver travels along the whole circle. (a) The final result; (b) Zoom in of (a) around the cylinder. In (b), it is clearer that the TD-BP also gets an inner bound and an outer bound of the cylinder's surface, which is in agreement with (1).

Next, a simulation is presented to show how multi-mode (multipath) propagation affects inverse scattering imaging. Here, the simulation's xOy horizontal configuration is similar to Fig.3 [35] and only increases R to 1 km. In the simulation, the water depth is 20 m while the source, the receiver and the rigid sphere are set to the same depth $z = 10$ m.

Because the sediment type is silt (mud), a high-loss bottom type, the number of effective propagation mode is 30, while that in sand sediment is 83 at 9 kHz. The first waveguide effect exerts on imaging in Fig.11(a) is the multi-path effect, causing multiple ambiguity lines. Here, "1" and "2" mark the first and second strongest ambiguity lines. Similar to the free-field case, as more receiving angles' data are added, the ambiguity lines "1" and "2" dwindle toward spots. The multi-path introduces defocusing ("1" and "2" fall in the white dashed contour) and sidelobe ripplings, "3" and "4"

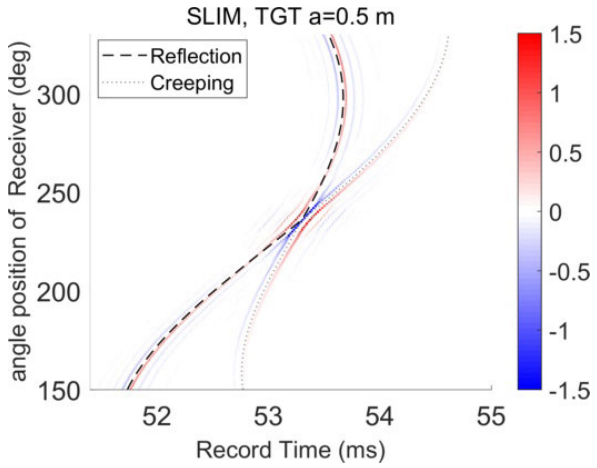

FIGURE 8. Similar to Fig.4, but use the SLIM algorithm to process.

in Fig.11(b). "4" is dimmer for more multi-path components coherently sum into a destructive interference. Fig.11(c) and Fig.11(d) "1" and "2" are strengthened as coherently accumulating more data while "3" and "4" are weakened. The structure in Fig.11(e) evolves that "1" becomes weaker and can be regarded as a defocused ghost spot of "2", while "5", a defocusing phenomenon, exhibits a parabolic shape. Also, there exist other patterns marked as "6". The previous sidelobes, "3" and "4", are further being diminished. In the final output, Fig.11(f), "3" and "4" are invisible, and "1" and "5" construct the defocusing and ghost of "2".

Fig.11 manifests that in an underwater waveguide, the multipath and group delay will cause severe image result degradation. The only way to solve this is to remove the CIR and rectify the received signals.

B. PHASE CONJUGATION-BASED CHANNEL DECONVOLUTION IMAGING METHOD

In Sec.III-A, it has been manifested that the multipath effect distorts the final ISCP images. However, (10) contains mode-coupling and cannot be easily resolved without vertically sampling the pressure field. According to [36], the scattering pressure of the rigid sphere can be expressed as

$$P_{\mathrm{sct}}(\mathbf{r}, \mathbf{r}_{\mathrm{s}}; \mathbf{r}_{\mathrm{t}}, \omega) \approx \frac{i}{4\rho(z_{\mathrm{s}})\rho(z_{\mathrm{t}})k} \left[\sum_{m=1}^{\infty} \psi_m(z)\psi_m(z_{\mathrm{t}}) \frac{\mathrm{e}^{ik_{rm}r}}{\sqrt{k_{rm}r}}\right] \times S(0, \phi; 0, \phi_{\mathrm{s}}) \left[\sum_{m'=1}^{\infty} \psi_{m'}(z_{\mathrm{s}})\psi_{m'}(z_{\mathrm{t}}) \frac{\mathrm{e}^{ik_{rm'}r_{\mathrm{s}}}}{\sqrt{k_{rm'}r_{\mathrm{s}}}}\right]. \quad (14)$$

Thus, after successful localization, phase conjugation can be used to deconvolve the CIR. However, the phase conjugation method introduces a large number of sidelobes as in Fig.12, which uses the same simulation data in Fig.11. That calls a better solution to conduct inverse scattering imaging in the underwater waveguide.

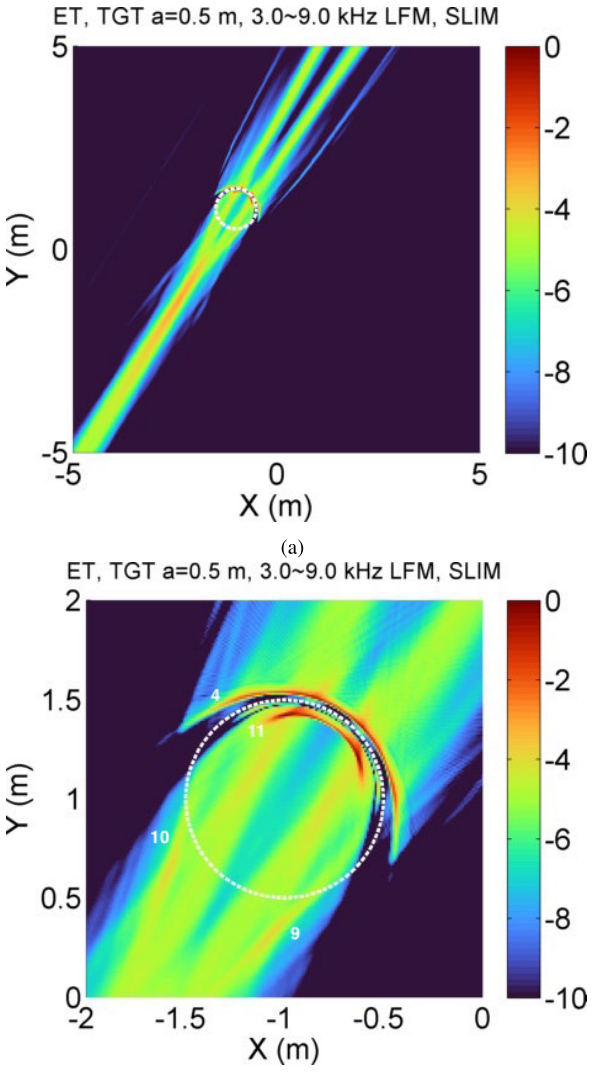

FIGURE 9. Similar to Fig.7, but use the SLIM method to process received data. (a) The final image; (b) Zoom-in of (a) around the cylinder. Compared with Fig.7, the image has at least lower the sidelobe with 2 dB. Also, the width of the ambiguity peaks in Fig.7 has been narrowed.

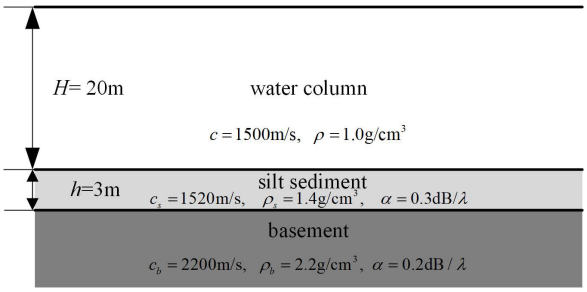

FIGURE 10. The environmental parameters used in the simulation.

C. SPARSE RECONSTRUCTION-BASED CHANNEL DECONVOLUTION IMAGING METHOD

In this paper, a sparse reconstruction based channel responce deconvolution imaging scheme is proposed to yield a clear ISCP output. Here, SLIM is used to find the multipath

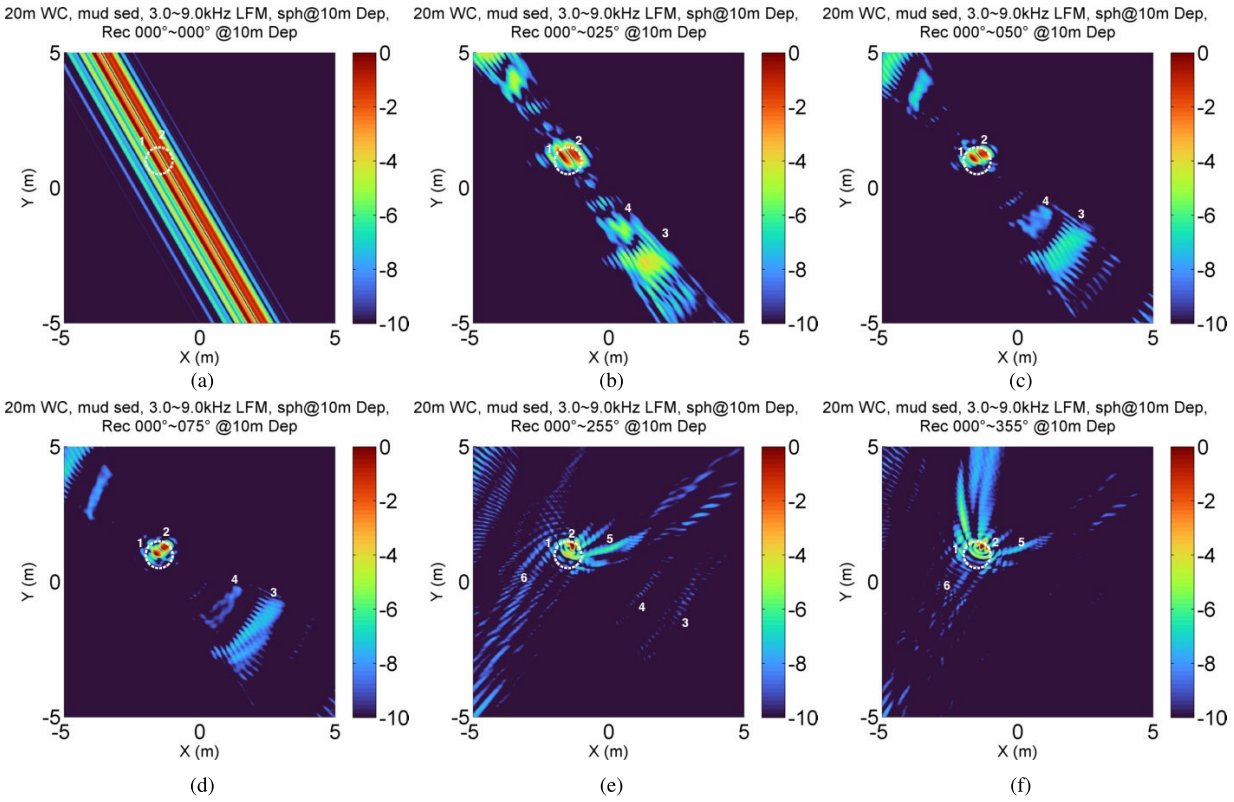

FIGURE 11. Imaging results when a spherical target in a 20 m depth range-independent waveguide; probing range $R = 1000$ m; source target and receiver are all at z=10 m depth, sediment type is mud. (a) The probing result when the source is at 0°; (b) Adding up six probing results from 0 – 25°; (c) Adding up 11 probing results from 0 – 50°; (d) Adding up 16 probing results from 0 – 75°; (e) Adding up 52 probing results from 0 – 255°; (f) Adding up all 72 probing results from 0 – 355°.

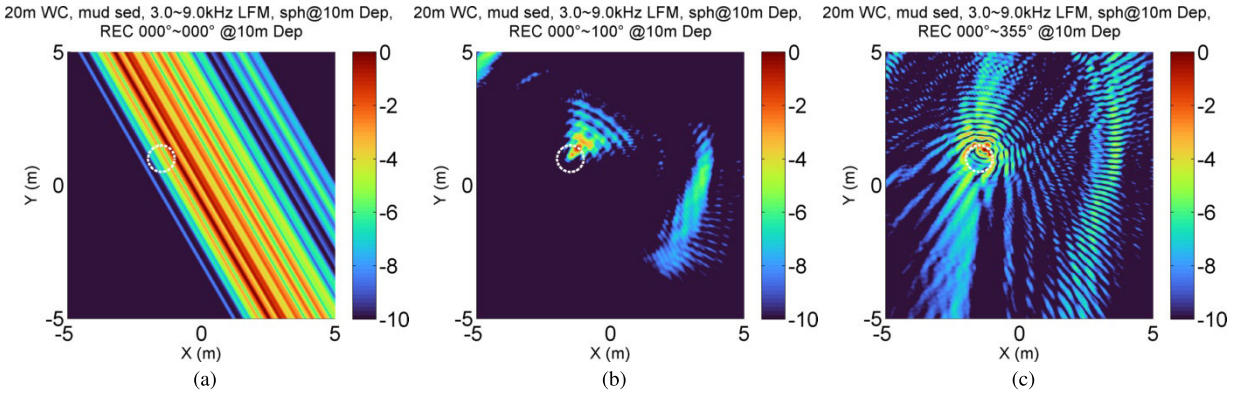

FIGURE 12. Inverse scattering imaging uses phase conjugation based channel response deconvolution in a waveguide environment. (a) Only use the 0° probing result; (b) Adding up 21 probing positions; (c) Adding up all 72 probing positions.

components at each receiver. The SLIM has a better time delay resolution than MF. For the same simulation data in Sec.III-A, the MF and SLIM output comparisons are displayed in Fig.13. Fig.13 shows that both MF and SLIM can find three main paths, but SLIM also gives the amplitude's polarity. When examining the receive data excited by the source at 0° as Fig.13(c), MF's output has a strong sidelobe, while SLIM exhibits a better time and amplitude resolution. In the simulation, the time resolution is 1/6 ms because a 6 kHz bandwidth signal is used. Due to the long propagation range, the delay between two neighbor paths is larger than 1/6 ms. Fig.13 also tells that the creeping wave is hardly caught in the backward scattering direction, and indicates that creeping waves will contribute less in imaging. This naturally requires a larger far-field transmit and receive aperture to generate a complete image.

All the paths found by SLIM are marked and categorized in Fig.14(a). The categorization standard includes the

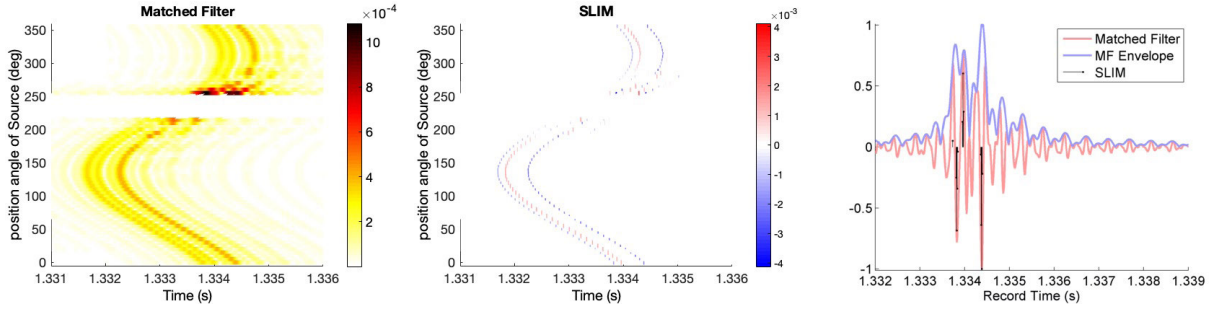

FIGURE 13. MF and SLIM output comparisons. (a) The envelope of MF output; (b) SLIM output; (c) Comparison between MF's outputs and SLIM's, when the source at 0°.

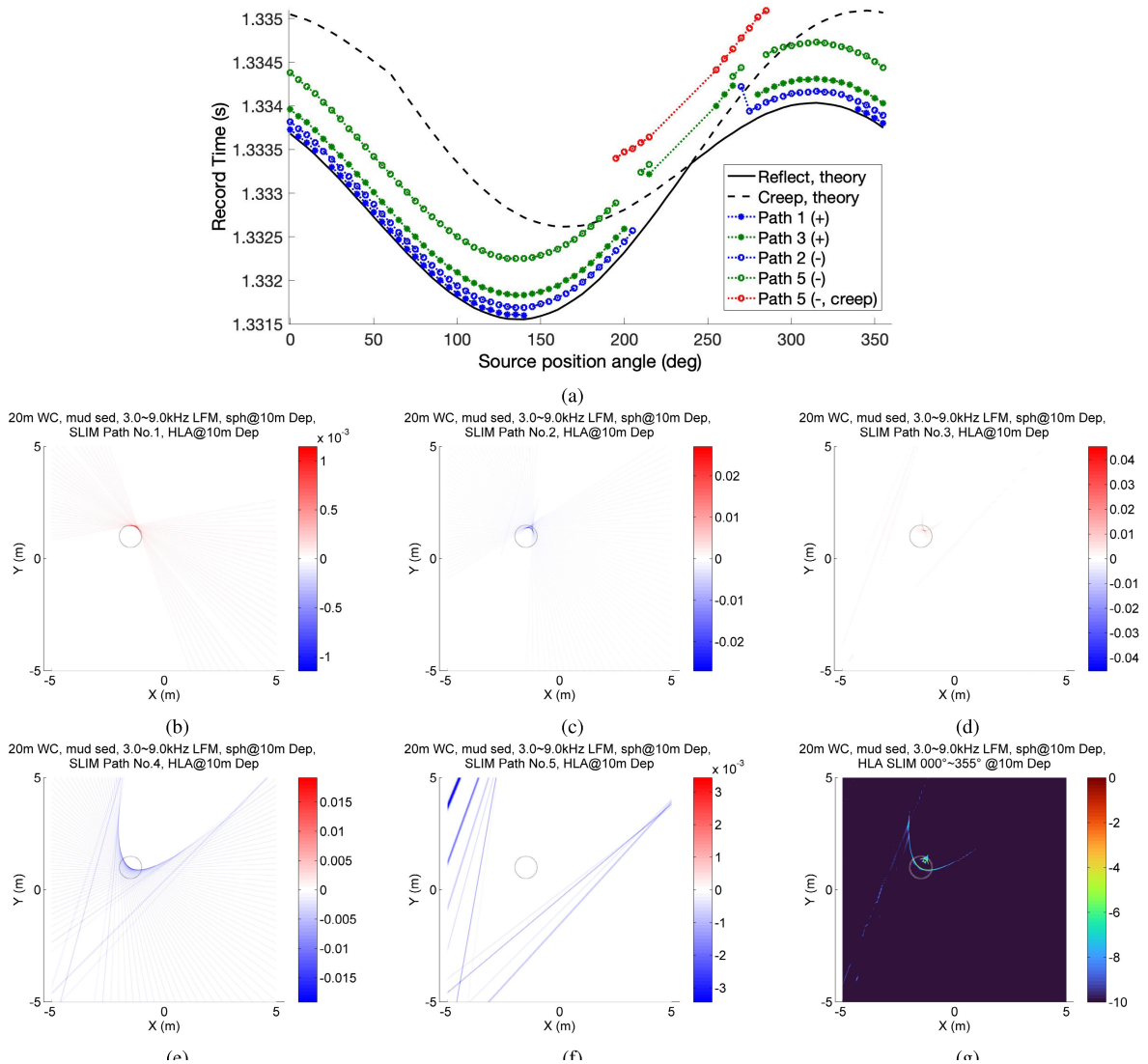

FIGURE 14. Inverse scattering imaging results analysis. (a) The identified path time of arrival (TOA). [Notes: The black solid line is the direct reflection path's TOA based on (7); The black dash line is the creeping wave's TOA based on (8); The "±" in figure legend indicates whether the path's amplitude is positive or not.] (b) Path 1's imaging result; (c) Path 2's imaging result; (d) Path 3's imaging result; (e) Path 4's imaging result; (f) Path 5's imaging result; (g) Superposition of all paths' in dB scale.

polarity of amplitude and TOA relative to theoretical reflection's TOA and creeping wave's TOA, which refer to (7) and (8). Fig.14(a) agrees with Fig.13 that most categorized paths are caused by reflection waves, corresponding to the free-field case's phenomenon that creeping wave is the dominant component when the bi-static scattering angle is less

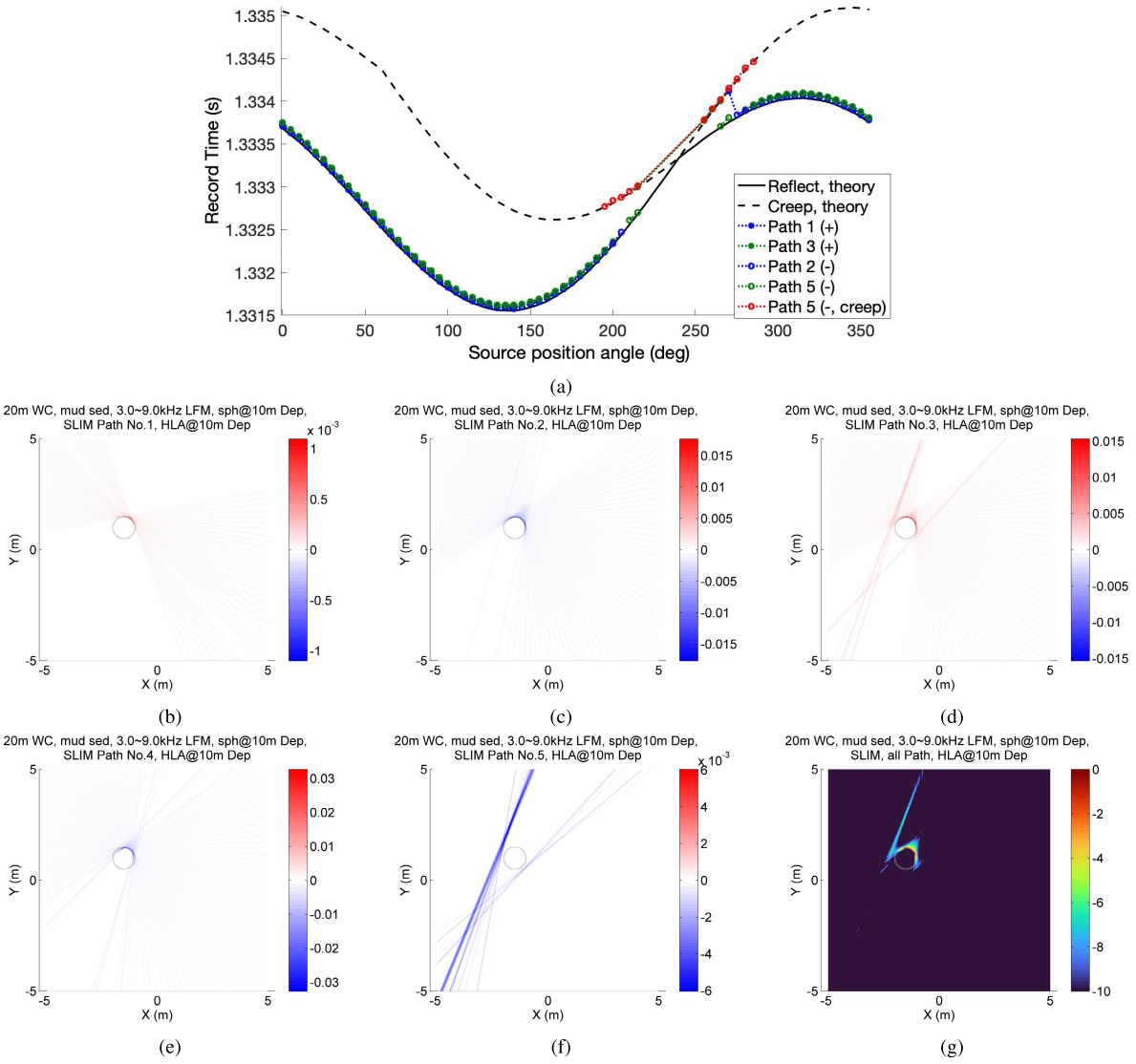

FIGURE 15. After time axis rescaled inverse scattering imaging results analysis. (a) The identified path time of arrival (TOA); [Notes: The black solid line is the direct reflection path's TOA based on (7); The black dash line is the creeping wave's TOA based on (8); The "±" in figure legend indicates whether the path's amplitude is positive or not.] (b) Path 1's imaging result; (c) Path 2's imaging result; (d) Path 3's imaging result; (e) Path 4's imaging result; (f) Path 5's imaging result; (g) Superposition of all paths' in dB scale.

than ±40°. Thus, the output images, Fig.14(b)-(e), correspond to Path 1-5, respectively. The black dash line marks the target's contour line in the imaging plane, and a red-blue color map is used to distinguish the positive or negative amplitude path's imaging result. The first path is a positive amplitude wave, which is close to the theoretical reflection delay, resulting in the enveloping surface is on the contour line of the target (Fig.14(b)). The remaining paths have significant lags, therefore, making the enveloping surfaces in each image moving into the target's contour line. The enveloping surface in Fig.14(c) generated by the second path is still a circular arc with a smaller radius. When the time lag goes larger, the enveloping surface starts shrinking toward a point (Fig.14(d)) and then expands to a parabola (Fig.14(e)). For the paths corresponding to creeping waves, they suffer less identified parts and large time lags and only map into lines away from the target's contour (Fig.14(f)).

Group speed can help build the relation between path's TOA and normal modes propagation. The mth mode's group speed c_{gm} approximates to [37]

$$c_{gm}^{-1}(\omega) = \frac{\mathrm{d}k_{rm}}{\mathrm{d}\omega} \simeq \frac{\omega}{k_{rm}} \int_0^H \frac{\psi_m^2(z)}{\rho(z)c^2(z)}\,\mathrm{d}z. \tag{15}$$

In our simulation, the sound speed in the water column is constant, so that (15) can be simplified as

$$c_{gm}(\omega) = c^2 \frac{k_{rm}}{\omega} \tag{16}$$

The expression above tells that the mth mode's group speed c_{gm} can be derived from its corresponding horizontal wavenumber k_{rm}. For the 3-9 kHz chirp signal, we take its center frequency 6 kHz as the reference and calculate the horizontal wavenumber. Thus, the paths distinguished by the SLIM algorithm has the following relation to the normal modes. Path 1 (blue "$*$" line in Fig.14(a)) corresponds to reflection wave's the first mode; Path 2 (blue "$\circ$" line) matches the reflection wave's the second mode; Path 3 (green "$*$" line) is the reflection wave's the third mode. Path 4 (green "$\circ$" line) is the reflection wave's the fifth mode; Path 5 (red "$\circ$" line) corresponds to the creeping wave, and its TOA matches Mode 5. Mode 4 is not identified by SLIM or MF. Mode with even number has a zero at target depth and Mode 4's derivative at the target depth is much smaller than the vertical wavenumber, making it harder to find its path. When the bi-static scattering angle is smaller than 20°, the reflection wave becomes weaker and the creeping wave should be more possibly identified. However, in the simulation, SLIM missed the first three modes at most bi-static scattering angles less than 20°. This phenomenon can be a further topic to study the physics behind that and will not be discussed hereafter.

Actually, in the dispersive propagation media, the same mode has a different group speed value across the signal band. Both SLIM and MF ignore that effect. Inter-mode components are weaker than intra-mode components as stated in [38]. This section follows this point and treats the identified path propagated from the intra-mode coupling. The propagation time delay can be transformed from phase term $\exp(ik_{rm}R)$ in (14). The propagation delay at frequency ω, nearly equals to group delay.

$$t_m(\omega) = \frac{k_{rm}R}{\omega} \tag{17}$$

Thus, for each path component, a rectified time axis will let the path's TOA move back toward its own free-field's theoretical prediction as (7) and (8). The time axis transform of the mth mode is given as:

$$t'_m = t\frac{c_{gm}}{c} \sim t\frac{k_{rm}}{k}. \tag{18}$$

Since SLIM neglects the dispersion, time axis scaling still takes wavenumbers at 6 kHz as reference. Fig.15(a) denotes each path's TOA value after TOA rectification. In Fig.15(a), all the identified paths move near the theoretically predicted values. All five transformed paths generate their new inverse scattering imaging as Fig.15(b) to Fig.15(f). These figures clearly show that after time rescaling, the enveloping surfaces are on the target's contour or tangent with the contour. The final output, which combines all the five paths, as shown in Fig.15(g), manifests that the sparse reconstruction based deconvolution method can generate an inverse scattering imaging result with lower sidelobe levels.

IV. CONCLUSION

This paper focuses on the inverse scattering imaging problems in a bistatic active sonar imaging. The time-domain back-propagation method is used for broadband signal probing cases. Moreover, combined with SLIM in two-dimensional free-field space, TD-BP not only reduces more sidelobe and raises at least a 2 dB peak-to-background ratio. The commonly used inverse scattering imaging methods will encounter defocusing and multiple ghosting introduced by a multipath effect in a shallow water environment. This problem is solved by using the SLIM algorithm, which is a sparse reconstruction method to identify the significant propagating paths. The identified paths are tagged into their possible categories, then rectified in the time domain. The proposed method achieves the effect of CIR deconvolution and yields a final low sidelobe inverse scattering image. Simulations in two-dimensional free-field space and three-dimensional range-independent waveguide are done to validate the methods developed in this paper.

REFERENCES

[1] S. F. Morse, P. L. Marston, and G. Kaduchak, "High-frequency backscattering enhancements by thick finite cylindrical shells in water at oblique incidence: Experiments, interpretation, and calculations," *J. Acoust. Soc. Amer.*, vol. 103, no. 2, pp. 785–794, Feb. 1998.

[2] M. Tran-Van-Nhieu, "Scattering from a ribbed finite cylindrical shell," *J. Acoust. Soc. Amer.*, vol. 110, no. 6, pp. 2858–2866, Dec. 2001.

[3] J. A. Bucaro, H. Simpson, L. Kraus, L. R. Dragonette, T. Yoder, and B. H. Houston, "Bistatic scattering from submerged unexploded ordnance lying on a sediment," *J. Acoust. Soc. Amer.*, vol. 126, no. 5, pp. 2315–2323, Nov. 2009.

[4] J. A. Bucaro, B. H. Houston, M. Saniga, L. R. Dragonette, T. Yoder, S. Dey, L. Kraus, and L. Carin, "Broadband acoustic scattering measurements of underwater unexploded ordnance (UXO)," *J. Acoust. Soc. Amer.*, vol. 123, no. 2, pp. 738–746, Feb. 2008.

[5] J. A. Bucaro, L. Kraus, B. H. Houston, H. Simpson, and A. Sarkissian, "Forward scatter target strength extraction in a marine environment," *J. Acoust. Soc. Amer.*, vol. 129, no. 6, pp. 3453–3456, Jun. 2011.

[6] S. Dey, A. Sarkissian, H. Simpson, B. H. Houston, F. A. Bulat, L. Kraus, M. Saniga, and J. A. Bucaro, "Structural-acoustic modeling for three-dimensional freefield and littoral environments with verification and validation," *J. Acoust. Soc. Amer.*, vol. 129, no. 5, pp. 2979–2990, May 2011.

[7] K. L. Williams, S. G. Kargl, E. I. Thorsos, D. S. Burnett, J. L. Lopes, M. Zampolli, and P. L. Marston, "Acoustic scattering from a solid aluminum cylinder in contact with a sand sediment: Measurements, modeling, and interpretation," *J. Acoust. Soc. Amer.*, vol. 127, no. 6, pp. 3356–3371, Jun. 2010.

[8] A. L. España, K. L. Williams, D. S. Plotnick, and P. L. Marston, "Acoustic scattering from a water-filled cylindrical shell: Measurements, modeling, and interpretation," *J. Acoust. Soc. Amer.*, vol. 136, no. 1, pp. 109–121, Jul. 2014.

[9] H. Jia, X. Li, and X. Meng, "Rigid and elastic acoustic scattering signal separation for underwater target," *J. Acoust. Soc. Amer.*, vol. 142, no. 2, pp. 653–665, Aug. 2017.

[10] T. C. Yang and T. W. Yates, "Scattering from an object in a stratified medium. II. Extraction of scattering signature," *J. Acoust. Soc. Amer.*, vol. 96, no. 2, pp. 1020–1031, Aug. 1994.

[11] J. J. Hall, M. R. Azimi-Sadjadi, S. G. Kargl, Y. Zhao, and K. L. Williams, "Underwater unexploded ordnance (UXO) classification using a matched subspace classifier with adaptive dictionaries," *IEEE J. Ocean. Eng.*, vol. 44, no. 3, pp. 739–752, Jul. 2019.

[12] E. M. Fischell and H. Schmidt, "Supervised machine learning for estimation of target aspect angle from bistatic acoustic scattering," *IEEE J. Ocean. Eng.*, vol. 42, no. 4, pp. 759–769, Oct. 2017.

[13] A. J. Devaney, *Mathematical Foundations of Imaging, Tomography and Wavefield Inversion*. Cambridge, U.K.: Cambridge Univ. Press, 2012.

[14] B. G. Ferguson and R. J. Wyber, "Application of acoustic reflection tomography to sonar imaging," *J. Acoust. Soc. Amer.*, vol. 117, no. 5, pp. 2915–2928, May 2005.

[15] D. S. Plotnick, T. M. Marston, and P. L. Marston, "Circular synthetic aperture sonar imaging of simple objects illuminated by an evanescent wavefield," *J. Acoust. Soc. Amer.*, vol. 140, no. 4, pp. 2839–2846, Oct. 2016.
[16] D. S. Plotnick and P. L. Marston, "High frequency imaging and elastic effects for a solid cylinder with axis oblique relative to a nearby horizontal surface," *J. Acoust. Soc. Amer.*, vol. 140, no. 3, pp. 1525–1536, Sep. 2016.
[17] K. Baik, C. Dudley, and P. L. Marston, "Acoustic quasi-holographic images of scattering by vertical cylinders from one-dimensional bistatic scans," *J. Acoust. Soc. Amer.*, vol. 130, no. 6, pp. 3838–3851, Dec. 2011.
[18] F. Cakoni, D. Colton, and P. Monk, *The Linear Sampling Method in Inverse Electromagnetic Scattering*, vol. 80. Philadelphia, PA, USA: SIAM, 2011.
[19] H. F. Alqadah, "A compressive multi-frequency linear sampling method for underwater acoustic imaging," *IEEE Trans. Image Process.*, vol. 25, no. 6, pp. 2444–2455, Jun. 2016.
[20] C. Tsogka, D. A. Mitsoudis, and S. Papadimitropoulos, "Selective imaging of extended reflectors in two-dimensional waveguides," *SIAM J. Imag. Sci.*, vol. 6, no. 4, pp. 2714–2739, Jan. 2013.
[21] C. Tsogka, D. A. Mitsoudis, and S. Papadimitropoulos, "Partial-aperture array imaging in acoustic waveguides," *Inverse Problems*, vol. 32, no. 12, Dec. 2016, Art. no. 125011.
[22] P. Gerstoft, C. F. Mecklenbräuker, W. Seong, and M. Bianco, "Introduction to compressive sensing in acoustics," *J. Acoust. Soc. Amer.*, vol. 143, no. 6, pp. 3731–3736, Jun. 2018.
[23] P. Gerstoft, A. Xenaki, and C. F. Mecklenbräuker, "Multiple and single snapshot compressive beamforming," *J. Acoust. Soc. Amer.*, vol. 138, no. 4, pp. 2003–2014, Oct. 2015.
[24] G. F. Edelmann and C. F. Gaumond, "Beamforming using compressive sensing," *J. Acoust. Soc. Amer.*, vol. 130, no. 4, pp. EL232–EL237, Oct. 2011.
[25] A. Xenaki and P. Gerstoft, "Grid-free compressive beamforming," *J. Acoust. Soc. Amer.*, vol. 137, no. 4, pp. 1923–1935, Apr. 2015.
[26] C. R. Berger, S. Zhou, J. C. Preisig, and P. Willett, "Sparse channel estimation for multicarrier underwater acoustic communication: From subspace methods to compressed sensing," *IEEE Trans. Signal Process.*, vol. 58, no. 3, pp. 1708–1721, Mar. 2010.
[27] Y. Zhou, A. Song, F. Tong, and R. Kastner, "Distributed compressed sensing based channel estimation for underwater acoustic multiband transmissions," *J. Acoust. Soc. Amer.*, vol. 143, no. 6, pp. 3985–3996, Jun. 2018.
[28] E. Fernandez-Grande, A. Xenaki, and P. Gerstoft, "A sparse equivalent source method for near-field acoustic holography," *J. Acoust. Soc. Amer.*, vol. 141, no. 1, pp. 532–542, Jan. 2017.
[29] M. R. Bai, C. Chung, and S.-S. Lan, "Iterative algorithm for solving acoustic source characterization problems under block sparsity constraints," *J. Acoust. Soc. Amer.*, vol. 143, no. 6, pp. 3747–3757, Jun. 2018.
[30] H. Überall, R. D. Doolittle, and J. V. McNicholas, "Use of sound pulses for a study of circumferential waves," *J. Acoust. Soc. Amer.*, vol. 39, no. 3, pp. 564–578, Mar. 1966.
[31] B. Thierry, X. Antoine, C. Chniti, and H. Alzubaidi, "μ-diff: An open-source MATLAB toolbox for computing multiple scattering problems by disks," *Comput. Phys. Commun.*, vol. 192, pp. 348–362, Jul. 2015.
[32] K. Zhao, J. Liang, J. Karlsson, and J. Li, "Enhanced multistatic active sonar signal processing," *J. Acoust. Soc. Amer.*, vol. 134, no. 1, pp. 300–311, Jul. 2013.
[33] F. Ingenito, "Scattering from an object in a stratified medium," *J. Acoust. Soc. Amer.*, vol. 82, no. 6, pp. 2051–2059, Dec. 1987.
[34] G. Gaunaurd and H. Überall, "Relation between creeping-wave acoustic transients and the complex-frequency poles of the singularity expansion method," *J. Acoust. Soc. Amer.*, vol. 78, no. 1, pp. 234–243, Jul. 1985.
[35] N. C. Makris and P. Ratilal, "A unified model for reverberation and submerged object scattering in a stratified ocean waveguide," *J. Acoust. Soc. Amer.*, vol. 109, no. 3, pp. 909–941, Mar. 2001.
[36] P. Ratilal, Y. Lai, and N. C. Makris, "Validity of the sonar equation and Babinet's principle for scattering in a stratified medium," *J. Acoust. Soc. Amer.*, vol. 112, no. 5, pp. 1797–1816, Nov. 2002.
[37] F. B. Jensen, W. A. Kuperman, M. B. Porter, and H. Schmidt, *Computational Ocean Acoustics*. New York, NY, USA: Springer, 2011.
[38] T. C. Yang and T. W. Yates, "Scattering from an object in a stratified medium. I. Frequency dispersion and active localization," *J. Acoust. Soc. Amer.*, vol. 96, no. 2, pp. 1003–1019, Aug. 1994.

JINGNING JIANG received the B.E. degree in electronic and information engineering from the Dalian University of Technology, Dalian, China, in 2012. He is currently pursuing the Ph.D. degree with the College of Information Science and Electronic Engineering, Zhejiang University, Hangzhou, China.

XIANG PAN received the bachelor's degree in underwater acoustic electronic engineering from the Harbin Ship Engineering Institute, in 1989, the master's degree in underwater acoustic engineering from the China Ship Research and Development Academy, in 1998, and the Ph.D. degree in information and communication engineering from Zhejiang University, in 2003.

He was a Visiting Scholar with Concordia University, Canada, from June 2009 to September 2009, the University of Victoria, Canada, from April 2011 to April 2012, and the University of Connecticut, USA, from May 2014 to September 2014. He is currently an Associate Professor with Zhejiang University. His research interests include statistical signal processing, speech processing, pattern recognition, and image processing.

T. C. YANG received the Ph.D. degree in high-energy physics from the University of Rochester, Rochester, NY, USA, in 1971. He was a Pao Yu-Kong Chair Professor with Zhejiang University, Hangzhou, China. From 2012 to 2014, he was a National Science Counsel Chair Professor with National Sun Yat-Sen University, Kaohsiung, Taiwan. He spent a period of 32 years with the Dispersive Wave Guide Effects Group, Naval Research Laboratory, Washington, DC, USA, as the Head of the Arctic Section, the Head of the Acoustic Signal Processing Branch, and a Consultant to the division on research proposals. He is currently a Professor with Zhejiang University. He has pioneered matched mode processing for a vertical line array and matched-beam processing for a horizontal line array. His current research interests include environmental impacts on underwater acoustic communications and networking, exploiting the channel physics to characterize and improve performance, environmental acoustic sensing and signal processing using distributed networked sensors, methods for improved channel tracking and data-based source localization, geoacoustic inversions, waveguide invariants, effects of internal waves on sound propagation in shallow water, arctic acoustics, and so on. He is a Fellow of the Acoustical Society of America.